International Journal of Pharmacology

Int. J. Pharmacol. **2026**; 22(4): 49188
https://doi.org/10.31083/IJP49188

Research Article

Berberine-Cinnamic Acid Co-Crystal Effect in Ameliorating Ulcerative Colitis Might Be Regulated Through Modulation of Intestinal Barrier and Improved Intestinal Absorption

Mengmeng Li[1,†], Chaoyu Hu[1,†], Wenheng Gao[1], Yong He[2], Ye Yang[1,3,*], Dengke Yin[1,2,4,*], Song Tan[1,*]

[1]School of Pharmacy, Anhui University of Chinese Medicine, 230012 Hefei, Anhui, China
[2]Anhui Provincial Key Laboratory of Chinese Medicinal Formula, 230012 Hefei, Anhui, China
[3]Anhui Province Key Laboratory of Pharmaceutical Preparation Technology and Application, 230021 Hefei, Anhui, China
[4]Key laboratory of Xin'an Medicine, Ministry of Education, 230038 Hefei, Anhui, China
*Correspondence: Y.Yang@ahtcm.edu.cn (Ye Yang); yindengke@ahtcm.edu.cn (Dengke Yin); tansong_1515@ahtcm.edu.cn (Song Tan)
[†]These authors contributed equally.
Academic Editor: Mehmet Ozaslan
Submitted: 17 December 2025 Revised: 9 March 2026 Accepted: 18 March 2026 Published: 12 August 2026

Abstract

Background: Berberine (BBR) has therapeutic effects against ulcerative colitis (UC). However, the poor solubility and low bioavailability of BBR limit the clinical utility of the chemical. BBR-CA, a co-crystal formed by BBR and cinnamic acid (CA), displays markedly improved intestinal bioavailability. **Methods:** The characteristics of BBR-CA were determined to confirm the formation of the co-crystal via intermolecular forces. The C_{max} values of BBR-CA and BBR were compared in rat blood. The apparent permeability coefficients (P_{app}) were measured and compared in an *in vitro* intestinal model. The restoration of intestinal barrier function and the regulation of cytokine levels (IL-6, IL-8, and TNF-α) were further examined in UC mouse models following BBR-CA treatment. In addition, this study evaluated the molecular pathways regulating UC-associated inflammation using transcriptomic analysis of lipopolysaccharide (LPS)-challenged Intestinal Epithelial Cells-6 (IEC6) cells treated with BBR-CA. **Results:** The morphology of BBR-CA significantly differed from that of BBR and CA. *In vitro* experiments showed that the P_{app} of BBR-CA was significantly higher than that of BBR; *in vivo* pharmacokinetic studies in rats indicated that the C_{max} of BBR-CA was significantly higher than that of BBR. Moreover, BBR-CA exhibited enhanced anti-inflammatory activity and improved intestinal epithelial tight junction integrity *in vivo*. Consistent with these findings, BBR-CA exerted therapeutic effects against UC by enhancing anti-inflammatory activity and preserving intestinal epithelial tight junctions. Participation of the JAK2-STAT3 signaling pathway in the regulation of inflammation in UC was further confirmed. **Conclusions:** BBR-CA improves the intestinal absorption properties of BBR, at least in part, through regulation of the JAK2-STAT3 signaling pathway. This results in reduced inflammation and increased integrity of the intestinal epithelial tight junction, thereby alleviating UC.

Keywords: berberine; cinnamates; ulcerative colitis; drug delivery; intestinal absorption; tight junctions; Janus kinases; STAT3 transcription factor

1. Introduction

Inflammatory bowel disease (IBD) is a generalized relapsing colitis-type inflammatory gastrointestinal condition primarily characterized by intestinal mucosal inflammation [1]. Although the specific causes of this disease remain unclear, clinical observations of genetic predisposition have implicated immune defects. Additionally, impaired mucosal integrity, tissue oxidation injury, and changes in microbial composition due to imbalance [2]. *Coptis chinensis Franch* is a classic detoxifying botanical traditionally used to resolve damp heat and systemic fires. Berberine (BBR), a major bioactive isoquinoline alkaloid, is widely used as an over-the-counter drug in the treatment of multiple diseases, including bacterial infections, tumors, hyperlipidemia, hypertension, diabetes, and inflammation [3,4,5,6,7,8,9,10,11]. Clinical and preclinical evidence have demonstrated that BBR alleviates ulcerative colitis (UC) by targeting the inflammatory cascade. However, its clinical utility is severely constrained by intrinsic biopharmaceutical limitations such as poor lipid solubility and extremely low oral bioavailability [12].

Pharmaceutical co-crystallization has emerged as an innovative and highly effective crystal engineering strategy to overcome these pharmacokinetic limitations. Cocrystals formed via non-covalent interactions, including hydrogen bonding, between an active pharmaceutical ingredient and a suitable co-former can fundamentally alter the crystal lattice energy and supramolecular arrangement of the parent drug without modifying its covalent structure. This microstructural modification markedly reduces hygroscopicity, increases the dissolution rate, and improves transcellular permeability, ultimately enhancing intestinal absorption [13]. However, the selection of the co-former is critical when designing a co-crystal for a complex disease such

as UC; it should ideally offer synergistic therapeutic benefits rather than merely serve as an inert structural scaffold. BBR can form cocrystals with organic acids. This structural modification enhances the solubility of BBR, reduces its hygroscopicity, and improves its stability under high-temperature and high-humidity conditions [14,15].

Xie Li Tang, a classic prescription developed by Zhang Xichun for the treatment of dysentery, is composed of *Coptis chinensis* Franch and *Cinnamomum aromaticum* Nees. This prescription is safe and effective for the treatment of active UC [16]. Modern pharmacochemical investigations have uncovered a core feature of the traditional co-decoction of these two botanical medicines: the spontaneous formation of a natural precipitate. This precipitate primarily comprises acid–base complexes formed via ionic interactions between alkaline isoquinoline alkaloids and acidic organic components [17]. Critically, the BBR-CA supramolecular complex is not an artificial synthetic construct developed in the laboratory. Rather, it is the core intrinsic material basis underpinning the clinical efficacy of this classic herbal formulation. Drawing directly on this chemical insight from traditional co-decoction practices, we selected cinnamic acid (CA) as the ideal co-former for BBR. CA exhibits well-validated antibacterial, antioxidant, and antitumor bioactivities [18,19,20], which directly antagonize UC-induced severe oxidative stress and mucosal damage. Therefore, the BBR-CA co-crystal was designed to leverage two synergistic biopharmaceutical and pharmacological advantages: (i) to recapitulate the natural active complex to structurally overcome the intestinal absorption barriers of BBR; and (ii) simultaneously deliver a bioactive co-former with complementary activity to synergistically ameliorate intestinal inflammation. BBR-CA, which is formed through the co-crystallization of BBR and CA, confers anti-lipogenic effects by regulating the PI3K-AKT-mTOR-SREBP-1 pathway [21]. However, it remains unclear how effectively these cocrystals prevent UC.

In this study, we investigated the efficacy of BBR-CA treatment for UC. First, we analyzed the characteristics of BBR-CA. Subsequently, we explored the pharmacokinetics and intestinal absorption of BBR-CA *in vivo*. To investigate its regulatory mechanism, lipopolysaccharide (LPS)-induced inflammation in IEC6 cells was induced using inflammatory response experiments. The aforementioned model was used to evaluate the relationship between BBR-CA and the maintenance of cell polarity and protein network regulation in the intestine. Next, we established a mouse model of colitis to evaluate the therapeutic effect of BBR-CA on UC. In addition, we performed eukaryotic transcriptomic analysis to identify potential therapeutic targets of BBR-CA in UC. Our results suggest that BBR-CA not only enhances the intestinal absorption and bioavailability of BBR but also exerts anti-UC efficacy through its anti-inflammatory and barrier-protective properties both *in vivo* and *in vitro*.

2. Materials and Methods

2.1 Materials, Drugs, and Reagents

BBR (Shanghai, China). Proteins were detected using an occludin-specific antibody (ID: 502601). Claudin-1 antibody (343203) was purchased from ZEN Biotechnology Co. (Chengdu, China). Mass spectrometry grades of methanol, acetonitrile, and formic acid were used. Fetal bovine serum (FBS) was purchased from Hyclone Laboratories (New York, NY, USA). Hank's balanced salt solution (HBSS) and Dulbecco's modified Eagle's medium (DMEM; G4510-500 mL) were purchased from ServiceBio (Wuhan, China).

2.2 Animals

Healthy BALB/c mice (male, 20 ± 5 g) were obtained from Hangzhou Ziyuan Laboratory Animal Technology. All tests were conducted under specific pathogen-free conditions and in an environment without estradiol removal, in a constant light/dark cycle of 12 h on average. All procedures were approved by the Animal Ethics Committee of Anhui University of Chinese Medicine (Approval number: AHUCM-mouse-2022128) and conducted in accordance with the Laboratory Animal Welfare Guidelines. The study was carried out in accordance with the ARRIVE guidelines.

Sprague–Dawley male rats weighing 200 ± 30 g were obtained from the laboratory animal center in Shandong Province. The subjects were acclimated to the controlled environment (temperature, 22 ± 2 °C; humidity, 45%; photoperiod, 12 h/day). A minimum of 12 h of fasting was allowed before pharmacological intervention. All the protocols were approved by the Animal Research Ethics Committee of Anhui University of Chinese Medicine (ID: AHUCM-rats-2022086).

2.3 Cell Culture

Caco-2 adenocarcinoma (RRID: CVCL_0025) and IEC6 rat intestinal (RRID: CVCL_0343) cells were obtained from iCell Bioscience and Shanghai Zhong Qiao Xin Zhou Biotech, respectively. Caco-2 cells were cultured in DMEM supplemented with 10% FBS, 1% Neat AA, and antibiotics. High-glucose DMEM containing 12% FBS was used for IEC6 cells. Cultures were incubated at 37 °C under 5% CO_2. Regular routine strand-to-polymerase chain reaction identification, mycoplasma tests using the detection kit (to confirm strain characteristics), and consistency across other laboratory work bases [22]. IEC6 cells were stimulated with 2 μg/mL LPS for 24 h to establish an *in vitro* inflammation model.

2.4 Animal Modeling, Grouping, and Sampling

All 42 mice were divided into six groups: healthy controls, dextran sulfate sodium (DSS)-induced models, positive control (salazosulfapyridine, DSS+SAZ), mice treated with probiotics and low-dose probiotic combination at

specific time points, berberine group (DSS+BBR), cinnamic acid group (DSS+CA), and berberine cinnamate co-crystal group (DSS+BBR-CA). Following a 7-day adaptation, acute colitis was induced by administering 3% DSS in drinking water for one week to all mice except the healthy controls. For the following seven days, SAZ (200 mg/kg), BBR (100 mg/kg), CA (30 mg/kg), or BBR-CA (130 mg/kg) in aqueous suspension was orally administered to the mice. Saline was used as a vehicle control for the normal and DSS cohorts. During the 14-day study period, the body weight and disease activity index (DAI) were recorded at specified times daily. Mice were provided free access to food and drinking water for 14 days.

All invasive procedures and euthanasia at the experimental endpoints were conducted in accordance with animal ethics guidelines. We ensured a smooth conclusion for the experiment by administering an intraperitoneal injection of 50 mg/kg pentobarbiturate (0.5% w/v). Successful induction was confirmed by observing the complete absence of corneal and foot withdrawal reflexes, which were considered indicators of sufficient anesthesia. Euthanasia was induced via cervical dislocation. All procedures were designed to minimize animal suffering. Colonic tissue was dissected immediately after euthanasia. Portions of the colonic segments were rinsed with physiological saline and fixed in 10% neutral buffered formalin for subsequent histopathological analyses. The remaining tissue samples were promptly stored at –80 °C in ultra-low temperature freezers for molecular biological testing.

Two groups of rats (n = 6 per group) were administered either BBR (80 mg/kg) or BBR-CA (115 mg/kg) formulations containing 0.5% CMC-Na for pharmacokinetic assessment. These doses corresponded to clinical equivalents. After gavage, approximately 0.5 mL of blood was collected hourly between 0.083 h and 24 h. Low-dose pentobarbital was intravenously administered at 8–10 mg/kg body weight to induce light anesthesia; blood samples were subsequently collected. Isolated plasma was centrifuged for 10 min at low speed (4 °C). Each sample (2 µL) was vortexed for 120 s before LC-MS/MS quantification. After sampling, the animals were humanely euthanized with 100 mg/kg pentobarbital (1% w/v), and respiration and heartbeat subsequently ceased.

2.5 Preparation and Characterization of BBR-CA

BBR and CA (equimolar, 500 mg BBR) were completely dissolved in 30 mL methanol to synthesize the co-crystal. Vacuum-assisted evaporation was performed at 45 °C using a rotating disk evaporator, and samples were subsequently subjected to a 2-h drying process under vacuum at 40 °C. Further optimized yields for large-scale synthesis were obtained using methanol/ethyl acetate (Vapor Diffusion Method).

To determine the molecular structure of the co-crystals, Fourier Transform Infrared (FT-IR) spectra were collected using a Bruker EQUINOX 55 spectrometer equipped with KBr pellets. Each sample was scanned for a total of 32 times from 4000 to 500 cm^{-1} within a resolution of 0.2 cm^{-1}.

The thermal behavior was characterized using an SDT Q600 instrument in a continuous nitrogen environment. Sealed-in aluminum samples were progressively heated by gradually increasing the temperature from room temperature to 250 °C at a rate of 10 °C/min.

The surface morphology was characterized by attaching BBR, CA, or their co-crystals to the two sides of a double-sided conductive tape and depositing a thin layer of platinum. Next, images were acquired using a Thermo Scientific Volumescope 2 scanning electron microscopy (SEM) platform. Electron micrographs were obtained at an accelerating voltage of 10 kV for higher resolution.

2.6 Histopathological Analysis

To assess structural changes, distal colon sections (n = 6 per group) were fixed in 10% neutral buffered formalin solution for paraffin embedding. Sections with a thickness of 4 µm were cut, subjected to deparaffinization, and stained with standard hematoxylin-eosin. Tissue integrity and inflammation were quantified microscopically based on standardized histopathological indices.

2.7 Immunohistochemical (IHC) and Immunofluorescence (IF) Analyses

Following the same protocol while making necessary adjustments to the IHC and IF methods. Samples were deparaffinized, followed by heat-induced antigen retrieval for 20 min at a temperature above. To inhibit endogenous peroxidases and nonspecific binding, slides were treated with 3% H_2O_2 (Ambient Conditions) and a goat serum solution for 10 min under room temperature. Sequential incubation included primary antibodies (overnight at 4 °C) and goat anti-rabbit secondary antibodies (30 min). A DAB chromogenic development reaction and hematoxylin counterstaining were used for the final visualization. IHC staining was performed using IL-6, IL-8, TNF-α, JAK2, p-JAK2, STAT3, and p-STAT3 as primary antibodies. IF analysis was performed using primary antibodies against claudin-1 (1:200 dilution), occludin (1:200), and ZO-1 (1:100) to detect junctional proteins. Secondary labeling was performed using Cy3-conjugated IgG (1:300). Ten quantifiable stochastic fields were obtained for each group using an inverted fluorescence microscope. Subsequently, the optical density (IOD) of all groups was calculated by integrating the light distribution.

2.8 In Vivo Pharmacokinetic Analysis of BBR-CA

Rat plasma samples were thawed at room temperature, 100 µL of plasma was precisely aspirated, and 300 µL of methanol solvent containing the internal standard was added. The mixture was then vortexed and mixed for 1

min, followed by centrifugation at 4 °C for 10 min at 12,000 r/min. The appropriate amount of supernatant was aspirated for analysis.

An ABSciex UPLC analytical platform combined with a 5500 QTRAPT triple-quadruplex mass spectrometry detection method was used for BBR content determination. Detection was performed using MRM in the presence of positive ESI. The key source parameters were configured as follows: ionic spray voltage, 5500 V; auxiliary temperature, 500 °C; curtain gas pressure, 30 psi; and collision gas pressure, 10 psi. Multiple-reaction detection mode was used to quantify BBR at m/z 336.1–320.2 (DP 96.0 V, CE 41.0 V) and glipizide (internal standard) at m/z 446.3–321.3 (DP 104.0 V, CE 19.0 V). Chromatographic data processing was performed using the Analyst software (v1.6.2; Applied Biosystems/MDS SCIEX, Foster City, CA, USA). Molecular separation was performed using the ACQUITY UPLC BEH-C18 system (1.7 µm, 2.1 × 5 mm) pre-stationarity Column (2.1 × 5 mm) at room temperature. The separation system was maintained at an isocratic flow rate of 0.3 mL/min with a 75:25 (v/v) composition of acetonitrile–0.1% aqueous formic acid solution. In-depth validation was performed to confirm the reliability of the analytical results, including the sensitivity, linear range, recovery, matrix effects, precision, and stability.

Non-compartmental analysis using PK Solver 2.0 was utilized to derive key pharmacokinetic variables such as peak concentration (C_{max}), time to reach C_{max} (T_{max}), and area under the curve (AUC_{0-t}). In addition, the elimination half-life ($t_{1/2}$), mean residence time (MRT), and apparent clearance/volume (CLzF and VzF) were determined. All metrics are presented as the mean ± SD. Statistical significance between groups was evaluated using one-way analysis of variance (ANOVA); $p < 0.05$ or 0.01 denoted significant differences.

2.9 Permeability Testing of Rat Small Intestine in a Ussing Chamber

In vitro analysis was conducted using a Ussing chamber to investigate permeation through the intracellular pathway. The Ussing chamber is an instrument used to measure the permeability of epithelial membranes to ions, nutrients, and drugs. It comprises two baths separated by a piece of mucosa or a layer of epithelial cells. Specimens were obtained from SD male rats (8 weeks old; provided by Shandong Experimental Animal Center). SD rats were anesthetized after 12 h of fasting, and their intestinal tissues were dissected. Excised intestinal segments (approximately 3 cm long) were washed clean with water and incubated at room temperature in chilled Krebs–Ringer solution (K-ReB). The physiological solution (pH 7.3) contained 117 mM NaCl, 25 mM $NaHCO_3$, and 11 mM glucose, along with the following indispensable ions: 4.7 mM KCl, 2.5 mM $CaCl_2$, and 1.2 mM each of $MgCl_2$ and NaH_2PO_4. The temperature was maintained at 0–4 °C during the process to preserve tissue viability. A 1-cm section was cut on ice bath plate, the intestinal mucosa was mounted in two slides (P-2300 and P2305; window area, 0.50 cm^2; Physiological Instruments, California Co., USA) in a Eusebio chamber, 5 mL of K-R solution was added to both sides of the device, and a mixture of 95% O_2 and 5% CO_2 was continuously ventilated. The water bath temperature was maintained at 37.0 °C to preserve the biological activity of the intestinal mucosa. The K-R solution in the device was aspirated and discarded, and 5 mL of BBR solution or BBR-CA and K-R solution (mass concentration: 200 µg/mL) was added to the mucosal and plasma membrane sides, respectively. Five milliliters of sample were extracted from the plasma membrane for sample fluorescence detection at 15, 30, 45, 60, 75, 90, and 120 min after dosing; the temperature and volume of the K-R solution were immediately replenished.

The permeation parameters were as follows: Cumulative permeation (Q in µg), where A and B are the amount of added drug and sampling volume (mL). The apparent permeation coefficient (P_{app}, in cm/s), where C_0 represents the initial mass concentration of the drug in the donor region after its introduction, and S is the sum of all effective areas involved in molecular transport. The unit area transit rate in µg/cm^2/s, where indicates the slope obtained by linear regression of time-cumulative permeation.

2.10 BBR-CA Transport in the Caco-2 Cell Model

Caco-2 cells were inoculated into a 24-well Transwell plate (Corning Incorporated, New York, NY, USA) at a density of 1×10^6 cells/cm^2. The cells were incubated for 14 days. Dense monolayers were formed when the transmembrane permeability (P_{app}) of fluorescent yellow was $<0.5 \times 10^{-6}$ cm/s [23] and could be used for permeation experiments. To assess bidirectional transport, Caco-2 cells were treated with 50 µg/mL LPS for 6 hours. BBR or BBR-CA (10 µg/mL) was added to either the apical (AP) or basal (BL) compartment of a Caco-2 cell monolayer using HBSS as the opposing chamber. HBSS samples were collected from the receiver end at regular intervals (every 15–120 min) and immediately restored by adding an equal amount of heated fresh buffer. Fluorescence spectrophotometry was used to quantify the permeation, and subsequent derivatization was used to calculate the permeability ratio based on previously established formulas.

2.11 Establishment of an In Vitro Inflammation Model to Examine Cell Survival and Permeability

IEC6 cells were seeded into 96-well plates at an adjusted density of 2×10^5 cells/mL (100 µL/well). The supernatant was removed after a 24-h adherence period. Media containing LPS along with the following treatments were subsequently added: BBR (66 µg/mL), CA (34 µg/mL), a BBR+CA mixture (66 + 34 µg/mL), and BBR-CA co-crystals (100 µg/mL and 200 µg/mL, respectively). In each of the six wells containing the replicates, 10 µL of CCK-8

solution was added after 1 h. After 1 h of incubation, absorbance was measured at 490 nm using a spectrophotometer, and the percentage of live bacteria was calculated.

The 24-well Transwell chambers containing IEC6 cells cultured for 7 days were set up as the normal (Normal), model (LPS), LPS+BBR-CA (100 μg/mL), and LPS+BBR-CA (200 μg/mL) groups. The culture environment was maintained in a humidified state of 5% CO_2 at 37 °C for 6 h. Next, a 20 μg/mL fluorescein solution (400 μL) was added to the AP chamber. After a 2-h incubation, a 300 μg/mL aliquot was harvested from the BL receiving compartment. Fluorescence spectroscopy was used to determine the number of signals and calculate the permeability index of the membranes.

2.12 Determination of the Effect of BBR-CA on LPS-Induced Expression of Tight Junction Proteins in IEC6 Cells

IEC6 cell density was adjusted to 2.0×10^5 cells/mL and inoculated in 24-well plates (each well was accompanied by a crawl sheet). The normal (normal), model (LPS), LPS+BBR-CA, LPS+BBR+CA, LPS+CA, and LPS+BBR groups were set until the cells formed a monolayer and spread over the bottom of the wells. The original drug culture solution was aspirated and washed with phosphate-buffered saline (PBS). Specimen preparation was initiated at 20 min of chemical fixation in 4% paraformaldehyde. Samples were then washed twice with PBS. Permeabilization was performed for 15 min, and 0.2% Triton X-100 was added to facilitate antibody diffusion. The non-specific binding site was blocked by goat serum for 1 h at 37 °C. Next, the sections were equilibrated with a ZO-1 primary antibody (1:200) for 14 hat 4 °C. Second-level labeling, which included incubation in 4',6-diamidino-2-phenylindole (DAPI), was performed for 1 h at room temperature after heating in the dark. Finally, after preserving the sample signal, the sample was mounted using a fade-reducing agent, followed by fluorescence microscopy and data analysis using ImageJ software (Bethesda, MD, USA).

2.13 Eukaryotic Participatory Transcriptomics of LPS-Induced IEC6 Cells Treated With BBR-CA

2.13.1 Establishment of Cellular Models and Group Dosing Protocols

IEC6 cells grown in the logarithmic phase were stimulated using LPS (2 μg/mL) for 24 h. A cellular inflammation model was established, and the normal, LPS, LPS+BBR-CA (58 μg/mL), LPS+BBR (40 μg/mL), LPS+CA (18 μg/mL) groups were set up with three parallel copies in each group. The samples were collected 24 h after LPS administration.

2.13.2 RNA Extraction Using the Trizol Method

After one wash with PBS, the cells were harvested by scraping off the culture dish. Total RNA was isolated by adding 3 volumes of TRIzol reagent to the collected cell pellets. Thereafter, an appropriate amount of chloroform was added to the solution, shaken vigorously, and left until separate phases were formed. The cells were allowed to stand at room temperature for 3 min and subsequently centrifuged at 2000 rpm for 10–15 min at 4 °C. The supernatant was aspirated and mixed with 1 mL of ethanol at 75% concentration. The mixture was then centrifuged at 12,000 rpm for 3 min at 4 °C, and the supernatant was discarded. The mixture was allowed to stand at room temperature for 3 min to dry. Next, 30–100 μL of DEPC water was added, and the mixture was allowed to dissolve completely. An appropriate amount of sample was extracted for testing, and the remaining sample was stored at –80 °C.

2.13.3 Library Construction and Quality Control

Sequence libraries were constructed using the NEBNext Ultra RNA Library Preparation Kit (Illumina-compatible). We ensured that the molarities of all libraries met the rigorous requirements for qRT-PCR analysis. Standardized quantitative assessment demonstrated that all the test results met the strict functional concentrations (>2 nM) required for high-throughput sequencing.

2.13.4 On-Line Sequencing

Sequencing was conducted using the Synthesis mode, in which dNTP with fluorescent labeling, DNA polymerase, and junction primers are added for amplification, and the sequencer can obtain fluorescent signals to detect sequence information.

2.13.5 Data Quality Control

Initial images were converted to signals using CASAVA, and raw sequence data were produced in the FASTQ format. To guarantee high precision of subsequent analysis, a strict filtering pipeline was adopted for this dataset to remove adapter-damaged reads, low-quality segments, and unrecognizable sequences such as N cells.

2.13.6 Sequence Comparison to the Reference Genome

To facilitate read mapping, HISAT2 v2.0.5 was used to systematically build a genome index at this time point. Thereafter, the high-quality sequence pool (clean reads) was aligned with the standard reference to assess the genomic correspondence and distribution.

2.13.7 Quantification of Gene Expression

Gene reads were calculated using StringTie and subsequently combined with gene lengths to calculate FPKM.

2.13.8 Differential Expression Analysis

The DESeq2 package was used to determine differential gene expression in all comparison pairs. At least three independent replicate groups from Experiment 1 were used to verify data authenticity.

2.13.9 Differential Gene Enrichment Analysis

Differentially expressed genes (DEGs) were functionally annotated using the R package ClusterProfiler. Enrichment analysis was combined with Kyoto Encyclopedia of Genes and Genomes (KEGG) pathway datasets, and a special correction was made to address the potential gene length bias in enrichment.

2.14 Statistical Analysis

Statistical analysis was performed using SPSS 16.0 software (Chicago, IL, USA). Data are expressed as the means and standard deviations. To evaluate the differences, independent *t*-tests and one-way ANOVA were used to compare pairs and multiple groups pairwise. Statistical significance was set to $p < 0.05$.

3. Results

3.1 Characterization of BBR-CA

The chemical structure of BBR-CA is shown in Fig. 1A. The FT-IR spectra displayed that BBR showed an absorption peak at 3423 cm^{-1}, which is caused by OH stretching vibration. BBR had an infrared response feature with the C=C stretching mode located at 1632 and 1506 cm^{-1}. The unique peaks of the OH, C=O, and C=C vibrations for CA were located at approximately 3200–2500 cm^{-1}, 1685 cm^{-1}, and 1450 cm^{-1}, respectively. The formation of BBR-CA co-crystals no longer showed the 1685 cm^{-1} signal. Instead, it was replaced with an obvious absorption peak at approximately 1550 cm^{-1} (Fig. 1B).

The differential scanning calorimetry (DSC) graph of CA starts at 133.0 °C, with the obvious peak at 133.9 °C. At a heat absorption peak of 9.12 mW/mg, the inflection and termination points were observed at 133.8 °C and 135.7 °C, respectively (Fig. 1C). The DSC graph of BBR starts at 86.2 °C and contains multiple peak points at 101.6 °C, 144.6 °C, 167.4 °C, and 191.7 °C. The DSC graph of BBR-CA contains multiple peak points at 106.6 °C, 128.1 °C, 166.0 °C, and 193.6 °C. Additionally, the characteristic peak of CA disappears on the DSC curve of BBR-CA, which indicates co-crystal formation.

The SEM images accurately compared the morphological features of BBR-CA, BBR, and CA (Fig. 1D). The co-crystal in BBR-CA had a needle-like structure with a relatively large aspect ratio and a relatively complete and flat crystal plane. BBR had irregular, rounded, spherical, and elliptical shapes, and its morphology differed from that of the co-crystal. CA had a blocky structure and a rough plane.

3.2 BBR-CA demonstrates enhanced intestinal absorption in vitro and improved oral bioavailability in vivo compared with BBR

The oral absorptions of BBR and BBR-CA were compared using *in vivo* pharmacokinetic experiments to explore the function of BBR-CA. BBR-CA absorption was reflected in the blood concentration of BBR. The gavage doses of BBR-CA and BBR were calculated based on equimolar doses of BBR (**Supplementary Table 1** and Fig. 2A). The C_{max} of BBR-CA was higher than that of BBR. Additionally, substantial prolongations in the time required to reach the peak concentration (T_{max}) and the average retention time of the active ingredients were observed ($p < 0.05$), suggesting changes in the absorption and excretion profiles. The $t_{1/2}$, C_{max}, and AUC increased 1.88-, 6.22-, and 3.20-fold ($p < 0.05$).

The Ussing Chamber permeability results showed that permeability was approximately 7.6 times higher than that of BBR and increased over time. Moreover, the final concentration of BBR-CA in the mucosal bath increased to 798.3 ppb (Fig. 2B,C). The resistance values of the jejunal segment fluctuated within the normal range (106.74–156.02 Ω-cm^2) during the experiment, indicating the good bioactivity of the intestinal mucosa. These results indicated a significant increase in P_{app} for BBR-CA.

BBR and BBR-CA at the same concentrations showed different permeation trends in Caco-2 cells (Fig. 2D,E). The P_{app} of BBR-CA (2.68×10^{-5} cm/s) significantly increased on the AP–BL side of the Caco-2 monolayer compared with that of BBR (2.35×10^{-6} cm/s). The drug was considered to be readily absorbed at $P_{app} > 2.5 \times 10^{-5}$ cm/s. The BBR-CA was well-absorbed and the P_{app} increased 11.4-fold compared to that of BBR at a drug mass concentration of 10 μg/mL; this was consistent with the results of the Ussing Chamber experiment.

To further elucidate the mechanism underlying the enhanced intestinal permeability of BBR-CA, we determined the equilibrium solubility in Krebs–Ringer (KR) solution and the oil–water partition coefficient (LogP, a core indicator of lipophilicity) of BBR and BBR-CA (**Supplementary Table 2**). The equilibrium solubility of BBR-CA in KR solution was 0.1 mg·mL^{-1}, which was 2-fold higher than that of free BBR (0.05 mg·mL^{-1}). Meanwhile, the logP value of BBR-CA was 1.0015, in sharp contrast to –0.7446 for free BBR, demonstrating the markedly improved lipophilicity of BBR-CA after structural modification. The intestinal transmembrane absorption of oral drugs is predominantly governed by two key physicochemical properties: aqueous solubility and lipophilicity. The enhanced aqueous solubility of BBR-CA can maintain a higher concentration of the dissolved drug at the absorption interface of the intestinal epithelium, consequently providing a stronger concentration gradient driving force for transmembrane diffusion in accordance with Fick's law. The significantly improved lipophilicity enables BBR-CA to cross the phospholipid bilayer of the intestinal epithelial cell membrane more readily, which is a core contributor to the elevated P_{app} values observed in both the Caco-2 cell monolayer and Ussing Chamber models.

Collectively, these results demonstrate that BBR-CA exhibits significantly enhanced intestinal absorption and oral bioavailability compared with free BBR, which is

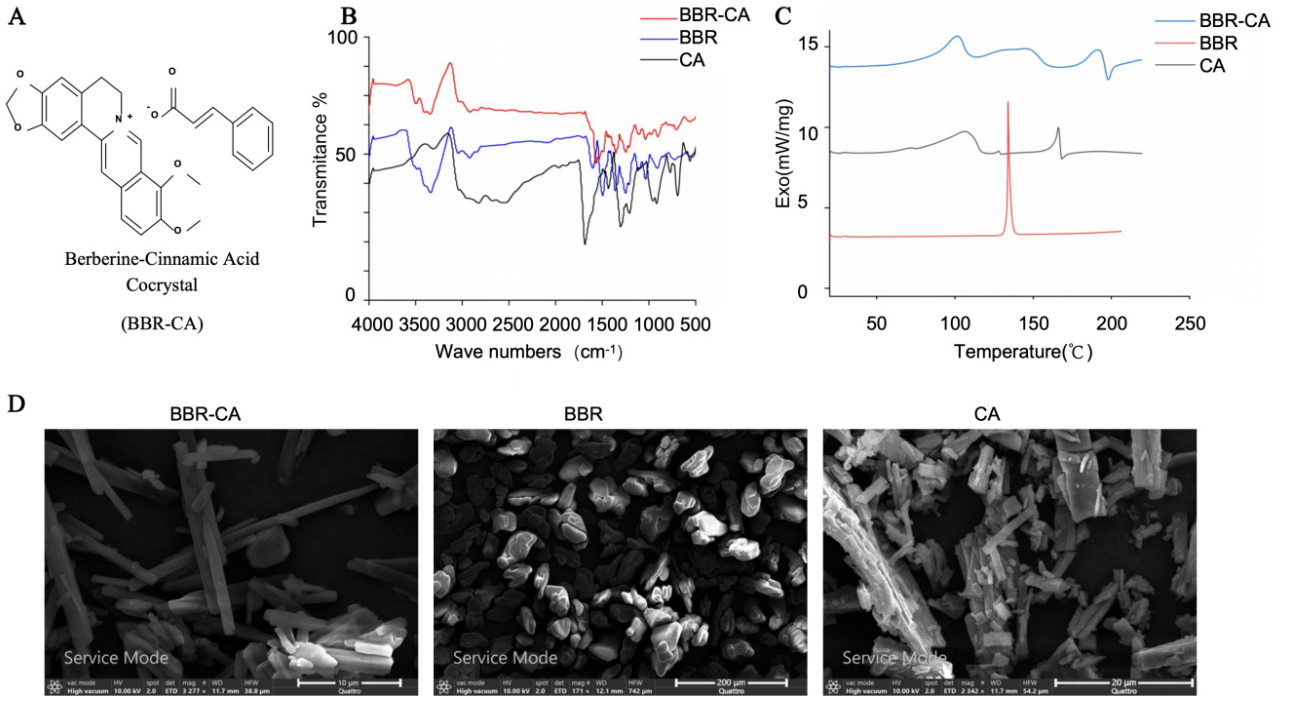

Fig. 1. Characterization of berberine-cinnamic acid co-crystal (BBR-CA). (A) The chemical structure of BBR-CA. (B) Fourier Transform Infrared (FT-IR) transmittance spectra of BBR-CA, BBR, and CA. (C) The exothermic processes of BBR-CA, BBR, and CA, as observed using differential scanning calorimetry (DSC). (D) Scanning electron microscopy (SEM) images of BBR-CA, BBR, and CA. Scale bars represent 10 μm, 200 μm, and 20 μm, respectively.

mainly attributed to the simultaneous improvement in aqueous solubility and lipophilicity.

3.3 BBR-CA Decreases LPS-Induced Inflammation and Permeability and Increases LPS-Reduced Expression of Tight Junction Proteins In Vitro

We first performed cell viability assays to validate the pharmacological advantages of the BBR-CA co-crystal formulation. LPS exposure markedly reduced the cell survival rate by approximately 49%. Although treatment with BBR or CA alone, as well as the BBR+CA physical mixture, conferred baseline cytoprotective effects, the BBR-CA co-crystal formulation achieved a significantly higher cell survival rate than the BBR+CA physical mixture (Fig. 3A). Concurrently, BBR-CA treatment effectively attenuated the LPS-induced elevation in epithelial monolayer permeability (Fig. 3B).

We subsequently quantified the anti-inflammatory potency of each formulation via ELISA. The expression of two core pro-inflammatory cytokines was assessed: TNF-α and IL-6. The BBR, CA, and BBR+CA physical mixture groups showed only moderate inhibitory effects on LPS-induced inflammatory responses. In contrast, the BBR-CA co-crystal displayed markedly enhanced anti-inflammatory activity, potently suppressing the pathological upregulation of both TNF-α and IL-6 expression (Fig. 3C,D).

Finally, we detected the expression of ZO-1, a core tight junction protein, by IF staining. LPS stimulation significantly downregulated ZO-1 expression and disrupted the structural integrity of tight junctions. Although all therapeutic interventions restored ZO-1 expression to varying degrees, the barrier repair effect of the BBR-CA cocrystals was significantly more robust than that of other treatment groups (Fig. 3E,F). Collectively, these results demonstrate that the BBR-CA co-crystal formulation alleviates cellular inflammation and restores the structural integrity of tight junctions.

3.4 Therapeutic Effect of BBR-CA on DSS-Induced Colitis in Mice

We established a mouse colitis model via oral gavage of 3% DSS for seven days to test the efficacy of BBR-CA. Concurrently, therapeutic interventions were administered over the same duration, with cohorts receiving SAZ, BBR, CA, or the BBR-CA co-crystal to evaluate their respective effects on DSS-induced intestinal inflammation. Compared with the normal group, the DSS group showed continuous weight loss with diarrhea and fecal bleeding (Fig. 4A). However, the mice administered SAZ, BBR, CA, or BBR-CA gradually recovered their body weights and showed reduced DAI scores (Fig 4A,B). DSS-induced colitis resulted in varying degrees of colonic shortening. Compared with the DSS-challenged group, colonic shortening was significantly alleviated by treatment with SAZ, BBR, CA, and BBR-CA (Fig. 4C,D). H&E-stained sections showed no

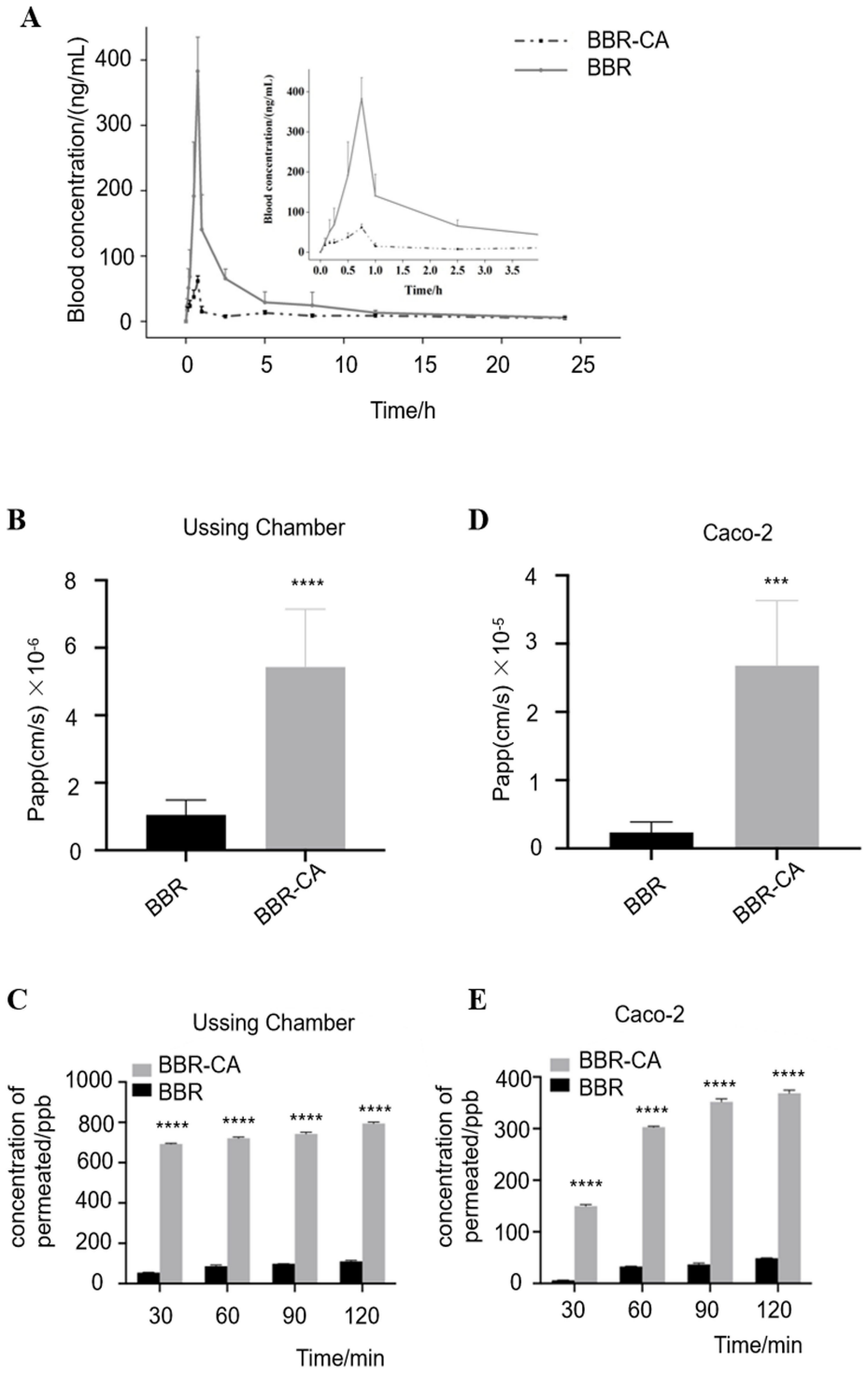

Fig. 2. ***In vivo*** **pharmacokinetic behavior and** ***in vitro*** **permeability of BBR-CA**. (A) Changes in the rat blood concentrations of BBR or BBR-CA over time after administration. The peak blood concentrations of BBR and BBR-CA between 0–3.5 h are clearly illustrated in the zoomed-in inset (n = 6, mean ± SD). (B) Permeation analysis of BBR and BBR-CA using the Ussing Chamber. (C) Detection of changes in drug permeation concentration over time using the Ussing chamber assay. (D) Permeation analysis of BBR and BBR-CA using the Caco-2 monolayer cell model. (E) Temporal fluctuations of drug permeability through the Caco-2 cell barrier. Stars indicate statistical differences among the two Groups ($p < 0.05$). $^{***}p < 0.001$ and $^{****}p < 0.0001$ indicate that there are significantly more severe deficiencies compared to the BBR group.

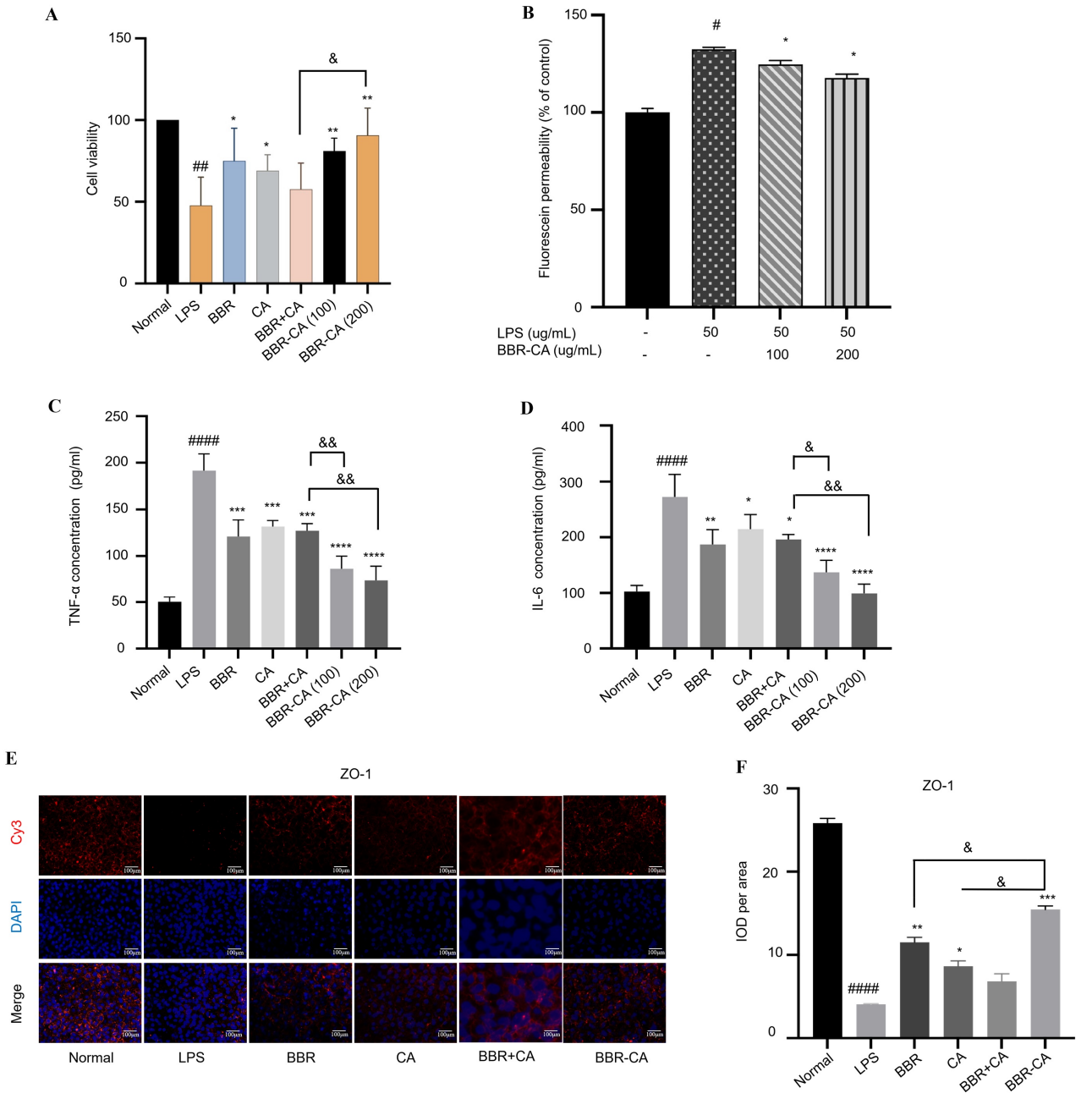

Fig. 3. Analysis of BBR-CA permeability and the effect of BBR-CA on ZO-1 expression *in vitro*. (A) CCK-8 analysis of cell survival under different drug treatments (n = 6, $\bar{x} \pm s$). (B) Detection of fluorescein permeability in lipopolysaccharide (LPS)-induced Caco-2 cells *in vitro* after drug treatment using Transwell (n = 3). (C) The expression level of TNF-α in LPS-induced IEC6 cells was detected by ELISA. (D) The expression level of IL-6 in LPS-induced IEC6 cells was detected by ELISA. (E) Immunofluorescence analysis of ZO-1 expression in LPS-induced IEC6 cells. Scale bar = 100 μm. (F) Quantification of ZO-1 protein expression (n = 3; $^{\#}p < 0.05$, $^{\#\#}p < 0.01$ versus the normal group; $^{\#\#\#\#}p < 0.0001$ compared with the normal group; $^{*}p < 0.05$, $^{**}p < 0.01$, $^{***}p < 0.001$, $^{****}p < 0.0001$ compared with the LPS group; $^{\&}p < 0.05$, $^{\&\&}p < 0.01$ versus the BBR-CA group).

structural disarray of the colonic epithelium in the control group; instead, they exhibited a well-organized tight junction system (Fig. 4E). The colonic tissues in the DSS group were significantly disrupted, mainly showing a disorganized texture, porous structure, distorted crypts, reduced goblet cells, and irregular arrangement of the intestinal epithelium. After treatment with SAZ, BBR, CA, or BBR-CA, the mice had a relatively intact crypt structure, more intact epithelial cells, and less inflammatory cell infiltration. Colonic dimension evaluation, body weight rebound,

and DAI indices suggest that BBR-CA exhibits a good therapeutic effect in DSS-induced colitis. As illustrated in Fig. 4F, BBR-CA was more effective in downregulating the expression of inflammatory factors than BBR and achieved the best anti-inflammatory effect.

3.5 The Effect of BBR-CA on Inflammatory Factors in DSS-Induced Colitis Mice

Pro-inflammatory factors such as TNF-α, IL-6, and IL-8, promote the development of inflammation in patients with IBD [2]. Levels of pro-inflammatory indicators such as TNF-α, IL-6, and IL-8 increased significantly in patients with UC but were reduced after drug treatment ($p < 0.05$; Fig. 5A–D). BBR-CA significantly reduced colonic IL-6 and TNF-α levels ($p < 0.01$) compared to BBR (Fig. 5B,D). These results indicated that BBR-CA has an improved inhibitory effect on DSS-induced colitis in mice.

3.6 Modulation of Tight Junctions Between Intestinal Epithelial Cells by BBR-CA

ZO-1, claudin-1, or occludin are membrane proteins associated with intestinal permeability barriers. They block the luminal antigen-activated colonic immunopathology during UC [24]. These proteins form a dynamic functional network in the intestine: Claudin-1 determines ion selective permeability; occludin regulates the macromolecular barrier, and ZO-1 integrates mechanical signals with cytoskeleton dynamics [25,26,27]. Representative IF images showed that the expression of claudin-1, occludin, and ZO-1 was reduced in the DSS group and rescued in the SAZ, BBR, CA, and BBR-CA groups (Fig. 6A). The BBR-CA group exhibited the most complete tight junction structure. Quantitative analysis showed that BBR-CA expression was significantly higher in intestinal epithelial tight junctions than BBR expression (Fig. 6B–D). Therefore, the BBR-CA group showed better regulation of tight junction structures than the BBR group.

3.7 BBR-CA Might Regulate the Inflammatory Response Through JAK-STAT3 Signaling Pathway

Intestinal epithelial dysfunction and activation of the inflammatory cascade are the core pathological hallmarks of UC. To determine the molecular mechanisms underlying the therapeutic efficacy of BBR-CA co-crystals, we performed genome-wide RNA sequencing (RNA-seq) and transcriptomic profiling of LPS-challenged IEC6 intestinal epithelial cells.

First, we identified DEGs across the three experimental groups: untreated normal controls, LPS-stimulated inflammatory model cells, and BBR-CA-treated LPS-challenged cells. LPS stimulation triggered genome-wide transcriptomic reprogramming, whereas BBR-CA treatment normalized the expression of most inflammation-associated genes, yielding a transcriptomic profile that clustered closely with that of healthy controls (Fig. 7A).

Biological classifications using Gene Ontology (GO) annotations and KEGG enrichment for signaling pathways were performed to elucidate the functional roles of these DEGs. The DEGs were predominantly enriched in biological processes central to inflammatory pathogenesis, including immune regulation, proinflammatory cytokine production, and cellular responses to inflammatory stimuli. KEGG enrichment further mapped these DEGs to multiple canonical inflammatory signaling cascades, with the most significant enrichment observed in the IL-17, NF-κB, TNF, Toll-like receptor, and JAK-STAT pathways (Fig. 7B).

Given the prominent enrichment of the JAK-STAT pathway, we performed a Gene Set Enrichment Analysis (GSEA) to validate the regulatory effects of BBR-CA on this cascade. The GSEA results were fully concordant with our KEGG findings. Gene sets associated with the global inflammatory response and JAK-STAT3 signaling were significantly upregulated in LPS-stimulated cells (Fig. 7C,D). Hierarchical clustering of core-enriched genes within the JAK2-STAT3 axis (including *ARG2*, *MMP9*, *CSF3*, *IFITM3*, and *CCL7*) confirmed that BBR-CA treatment markedly reversed the pathological upregulation of their expression (Fig. 7E).

The transcriptome was used to verify colonic JAK2/STAT3 signaling activity using IHC. Although total protein expression was stable across all groups, phosphorylated isoforms (p-JAK2 and p-STAT3) showed a significant increase in DSS-injured areas, confirming robust hyperactivation of the JAK2-STAT3 axis in colitis. Consistent with our *in vitro* transcriptomic data, oral administration of BBR-CA significantly downregulated p-JAK2 and p-STAT3 expression in colonic mucosal tissues (Fig. 7F,G). Collectively, these findings demonstrate that the anti-colitis efficacy of the BBR-CA co-crystals was mediated predominantly through targeted inhibition of the proinflammatory JAK2-STAT3 signaling pathway.

4. Discussion

In this study, we evaluated the physicochemical properties, potential anti-colitis effects, pharmacokinetic behavior, and permeation properties of BBR-CA *in vivo* and *in vitro*. The FTIR spectra of BBR-CA indicated strong interactions and the formation of crystals rather than simple mixtures. Furthermore, BBR-CA was a more stable cocrystal. This co-crystal had a needle-like structure with a relatively large aspect ratio and a relatively complete and flat crystal plane. The specific structure of BBR-CA may contribute to the enhanced intestinal absorption and bioavailability of BBR.

In a DSS-induced murine colitis model, both free BBR and BBR-CA ameliorated the macroscopic colitis phenotypes, including accelerated body weight recovery, restored colon length, and reduced DAI scores. However, BBR-CA exerted significantly superior efficacy in suppressing intestinal inflammation and reinforcing the epithelial bar-

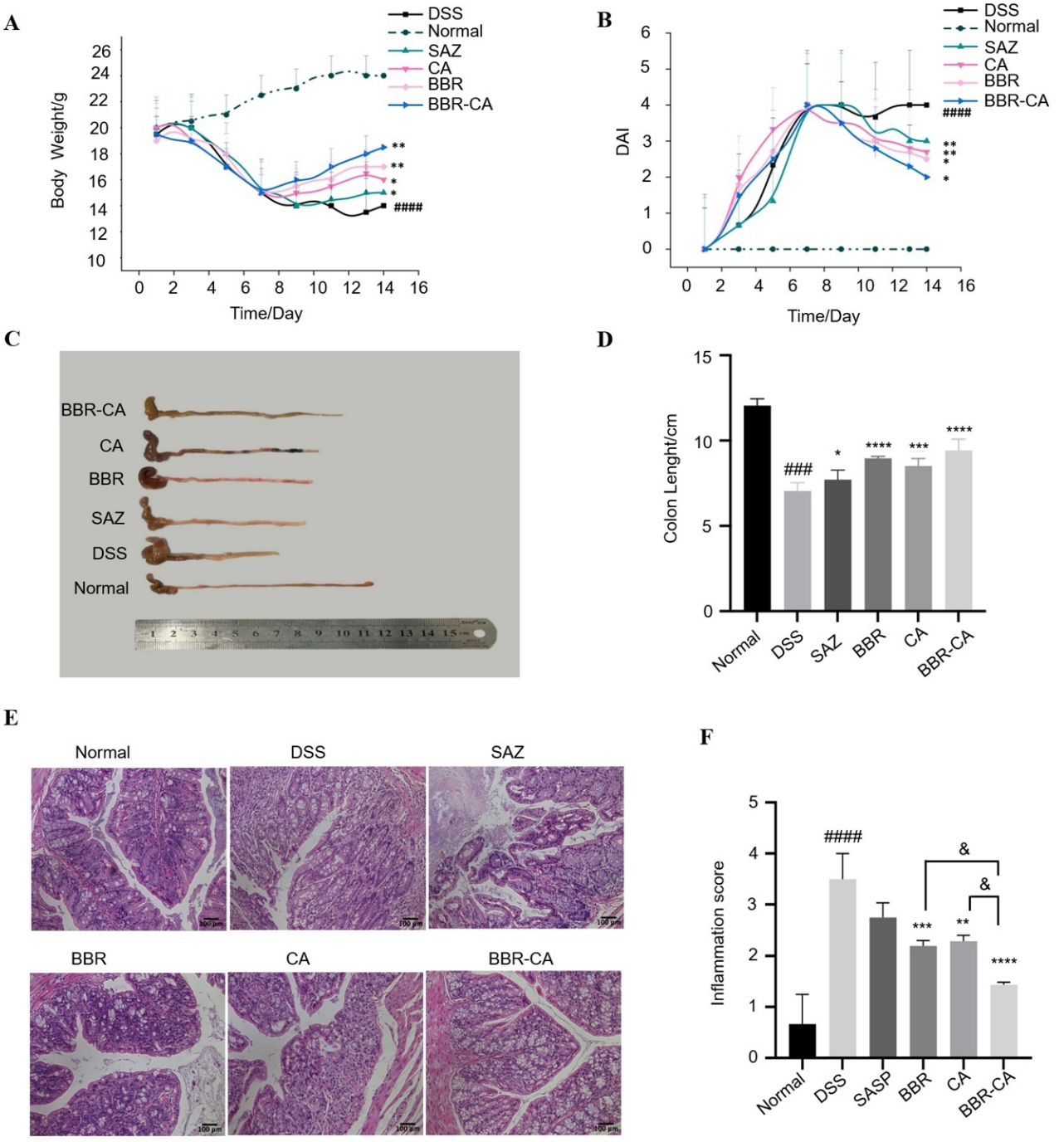

Fig. 4. BBR-CA promotes recovery of dextran sulfate sodium (DSS)-induced colitis in mice. (A) Longitudinal weight fluctuations during disease progression. (B) Terminal disease activity index (DAI) scoring post-intervention. (C) Macroscopic colonic images. (D) Measured colon lengths per group. (E) Tissue H&E staining (n = 6). Scale bar = 100 µm. (F) Inflammatory grades based on (E). $^{\#\#\#}p < 0.001$, $^{\#\#\#\#}p < 0.0001$ versus the normal group; $^{*}p < 0.05$, $^{**}p < 0.01$, $^{***}p < 0.001$, $^{****}p < 0.0001$ versus the DSS group; $^{\&}p < 0.05$ versus the BBR-CA group.

rier compared to free BBR or the BBR-CA physical mixture [28,29]. The intestinal epithelial barrier is the primary defense against luminal antigens, and its disruption drives massive immune cell infiltration and IBD progression [30]. Our study showed that the beneficial effects of BBR-CA could directly protect the intestinal epithelial barrier and were more effective than BBR. The aqueous extract of cinnamon reduces epithelial cell permeability and enhances tight junctions between epithelial cells [31]. Similarly, BBR exerts a protective effect in the colon via the Wnt/β-

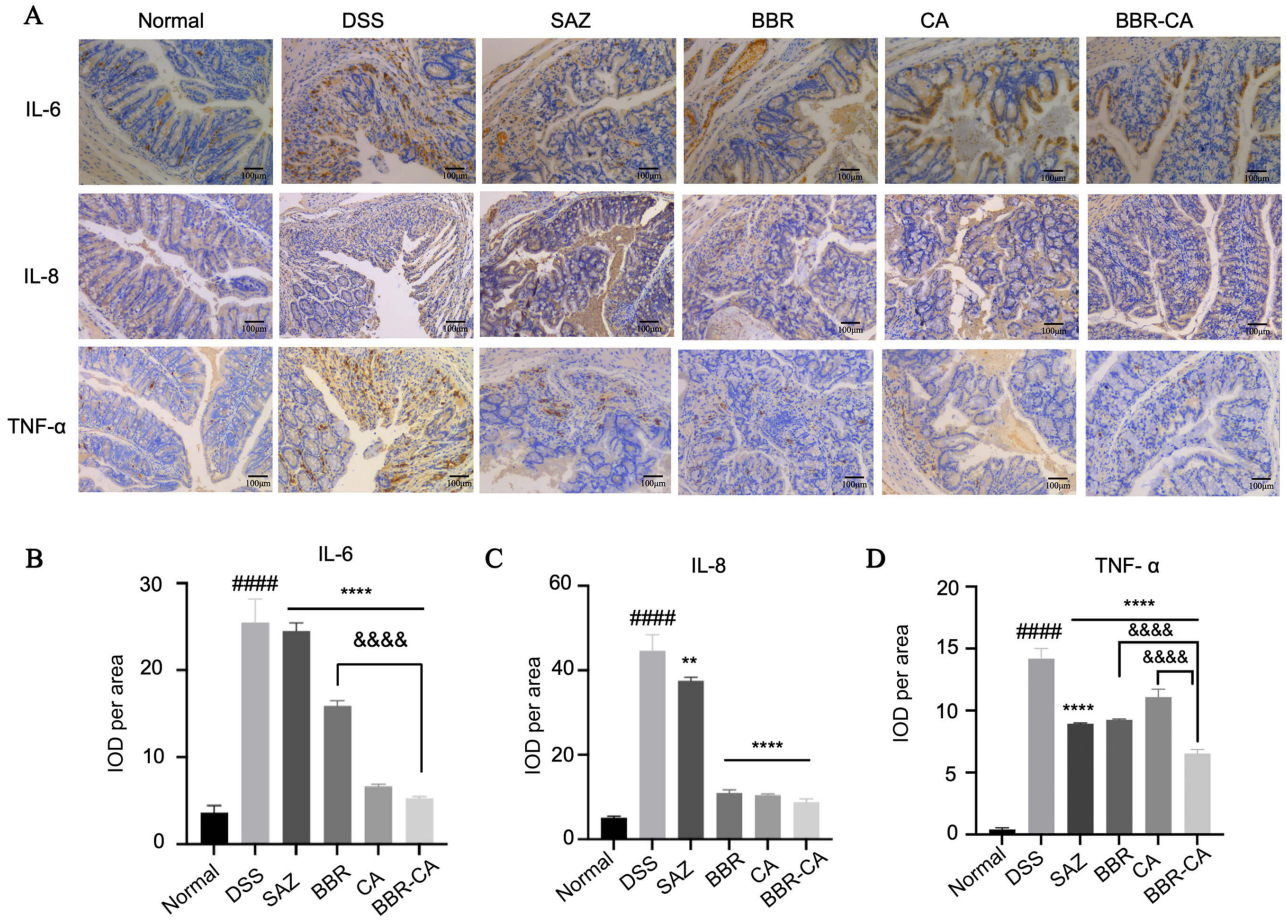

Fig. 5. BBR-CA reduces the horizontal expression of pro-inflammatory factors. (A) Representative immunohistochemical images of IL-6, IL-8, and TNF-α in the murine colon sections (scale bar = 100 μm). (B–D) Semi-quantitative IOD analysis of corresponding protein expression among different groups. $^{\#\#\#\#}p < 0.0001$ compared to the control group; $^{**}p < 0.01$ and $^{****}p < 0.0001$ versus the DSS group; $^{\&\&\&\&}p < 0.0001$ versus the BBR-CA Group.

catenin pathway [32]. Our data demonstrate that integrating these two phytochemicals into a single supramolecular co-crystal yields synergistic therapeutic effects. This co-crystal had far greater potency in restoring the tight junction proteins and inhibiting inflammatory cascades than simple co-administration of the two compounds. Consistent with our results, CA and BBR may exert a synergistic effect in protecting the intestinal epithelial barrier. In addition, CA modulates the inflammatory response of Th cells and macrophages, whereas BBR selectively enriches short-chain fatty acid-producing bacteria and reduces intestinal microbial diversity to improve gastrointestinal health [33]. These results indicate that BBR-CA exerts its anti-colitis effects through multiple pathways, including the protection of intestinal epithelial integrity and anti-inflammatory effects.

We performed unbiased transcriptomic profiling to define the mechanistic basis of these therapeutic effects. RNA-seq coupled with KEGG enrichment analysis and GSEA identified the JAK2/STAT3 signaling cascade as the core therapeutic target of BBR-CA. The JAK/STAT axis as a major regulator of IBD pathogenesis [34], and the clinical success of FDA-approved JAK inhibitors (e.g., tofacitinib) in UC further validates this pathway as a high-priority therapeutic target [35]. In mucosal injury, IL-6 and other pro-inflammatory cytokines trigger JAK2 transphosphorylation, consequently driving sequential STAT3 phosphorylation, nuclear translocation, and transcriptional activation of inflammatory genes. This creates a pathological positive feedback loop that amplifies the cytokine storm and sustains chronic inflammation [36,37]. Aberrant STAT3 hyperactivation also directly impairs epithelial restitution and represses the transcription and assembly of key tight junction proteins, rendering the hyperactivated JAK2/STAT3 axis a core driver of both the inflammatory dysregulation and barrier disruption that define UC.

In vivo IHC analysis confirmed that BBR-CA significantly inhibited the phosphorylation and activation of JAK2 and STAT3 in inflamed colonic tissues through synergistic dual-target action. BBR acts as a natural STAT3 inhibitor, but its *in vivo* efficacy is constrained by poor in-

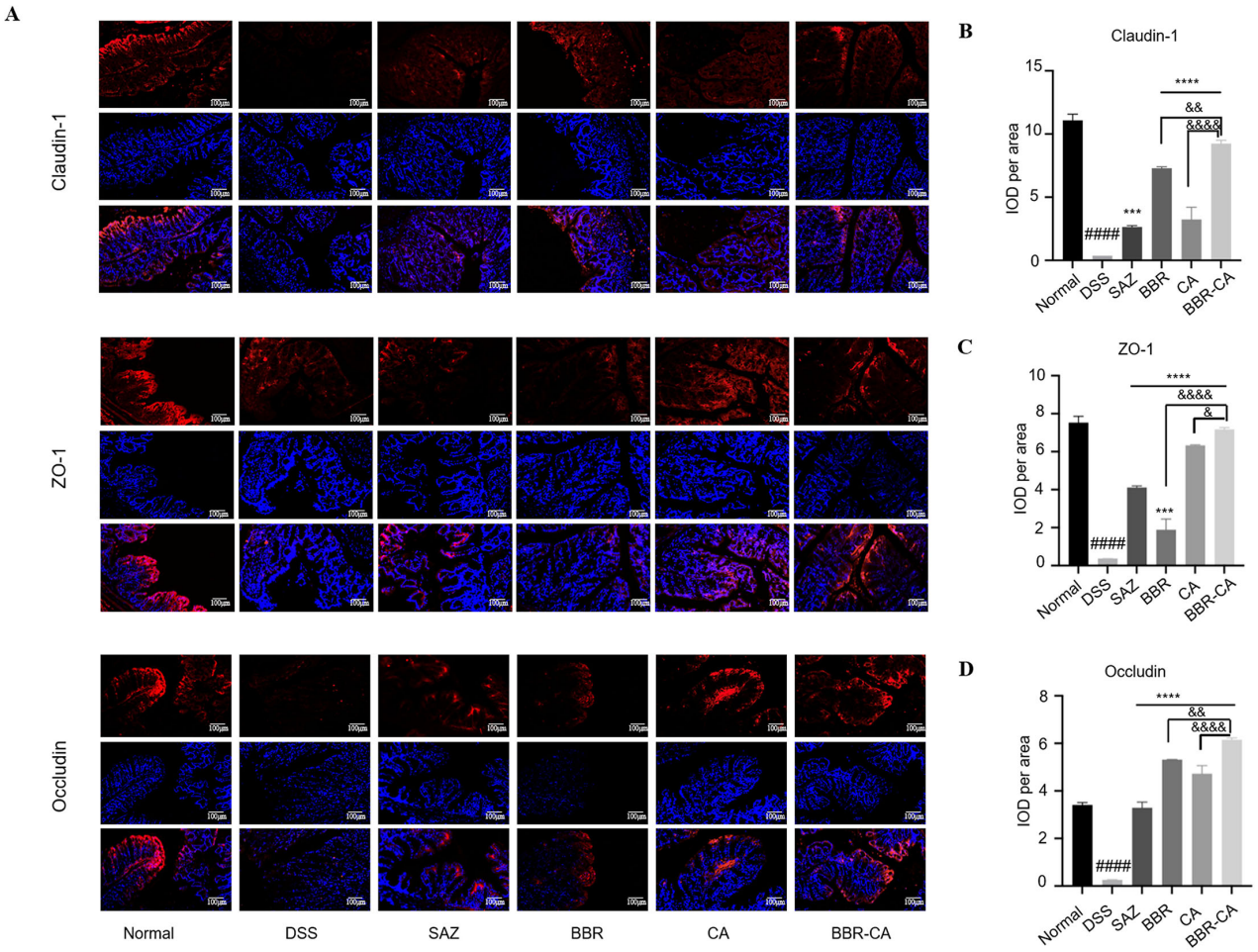

Fig. 6. BBR-CA improves intestinal epithelial barrier function. (A) Immunofluorescence analysis of claudin-1, occludin, and ZO-1 expression in the DSS of mice with colitis (n = 6). Scale bar = 100 μm. (B–D) Quantification of claudin-1, ZO-1, and occludin expression. $^{\#\#\#\#}p < 0.0001$ versus the normal group, $^{***}p < 0.001$ and $^{****}p < 0.0001$ versus the DSS group. $^{\&}p < 0.05$, $^{\&\&}p < 0.01$, and $^{\&\&\&\&}p < 0.0001$ versus the BBR-CA group.

tracellular accumulation. Contrastingly, CA scavenges reactive oxygen species, key upstream triggers of JAK activation [38]. Critically, the enhanced transcellular permeability of the co-crystal formulation delivered significantly higher intracellular concentrations of both active moieties at inflamed mucosal sites than the simple physical mixture, amplifying this synergistic blockade. These convergent transcriptomic and protein-level findings directly link the therapeutic efficacy of BBR-CA to targeted modulation of the JAK2/STAT3 axis rather than non-specific antioxidant effects. By interrupting this pathological feedback loop, BBR-CA simultaneously halted mucosal cytokine amplification and enabled robust structural restoration of the intestinal epithelial barrier.

UC is not only a localized inflammatory disease of the intestinal tract but also a systemic disease that manifests as an acute, chronic, and systemic relapsing gastrointestinal disorder, with an increasing incidence and prevalence worldwide [38,39]. Chinese herbal tonics can effectively improve the absorption of some insoluble ingredients, and the possible mechanisms involved include solubilization, emulsification, and micro- and nano-systems [40]. BBR-CA increased the intestinal absorption of BBR *in vitro* and *in vivo*. The T_{max} of BBR-CA was consistent with that of BBR. However, the $t_{1/2}$ and MRT_{0-24} of BBR-CA were significantly shorter than those of BBR, potentially because BBR-CA improves solubility and maintains the soluble form of BBR during dilution and permeation in the gastrointestinal tract. The potent anti-UC efficacy of BBR-CA arises from two synergistic and complementary advantages: optimized pharmacokinetic performance via crystal engineering, and targeted dual-pronged blockade of the pro-inflammatory JAK2/STAT3 signaling axis.

5. Limitations

Although the current study demonstrated the promising therapeutic potential of BBR-CA co-crystals against UC, several limitations should be noted when interpret-

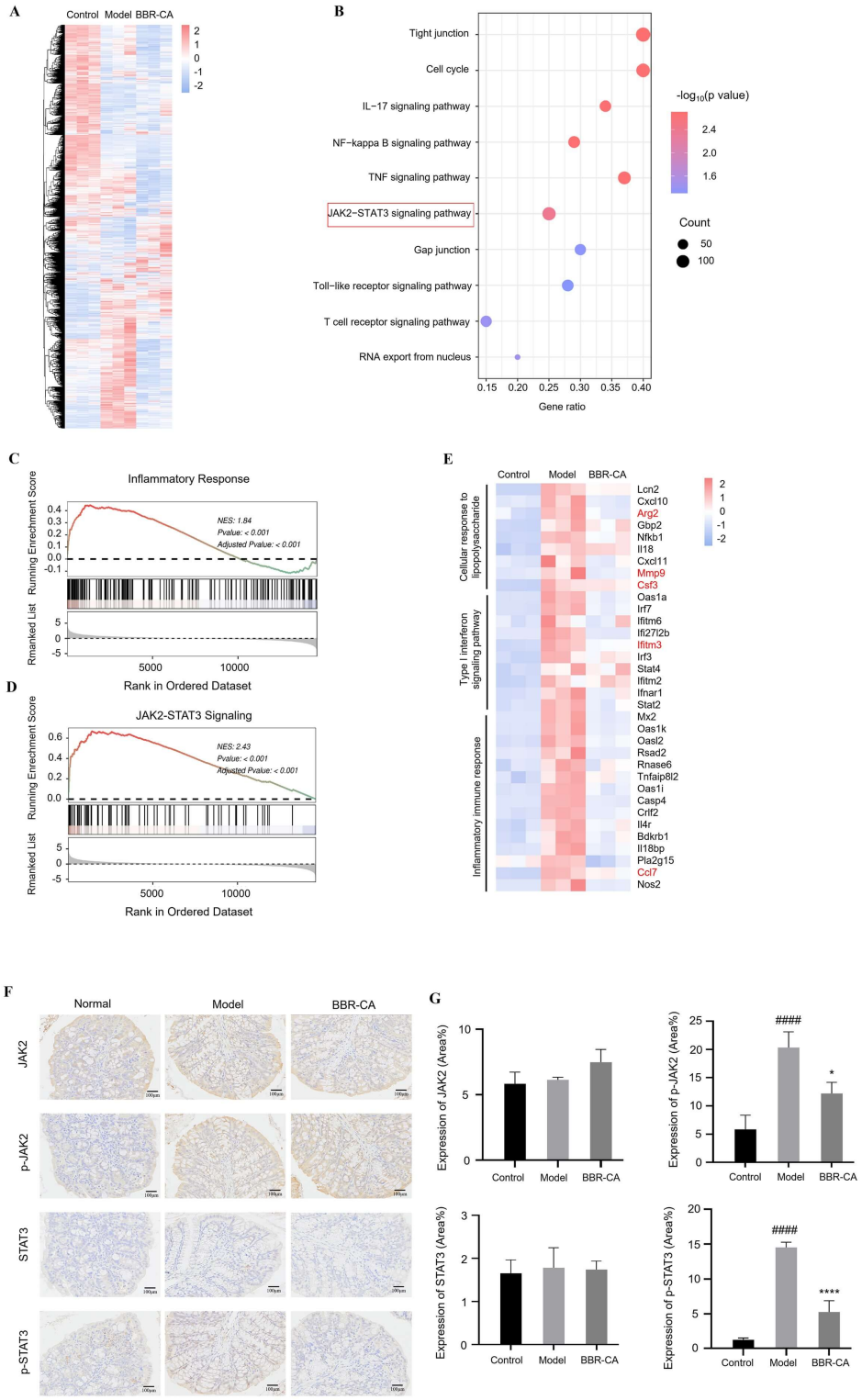

Fig. 7. Transcriptomics analysis of the effect of BBR-CA on LPS-treated cells. (A) Heatmaps of differentially expressed genes (DEGs) in different groups. (B) Gene Ontology term enrichment analysis of DEGs. (C,D) Genomic enrichment analysis (GSEA) of the signaling pathways involved in inflammatory responses and JAK-STAT3. (E) Heatmaps of genes whose expression was reduced by BBR-CA in LPS-induced models. (F) The expression levels of JAK2, p-JAK2, STAT3 and p-STAT3 in mouse intestinal tissues were detected by immunohistochemistry (Scale bar: 100 μm). (G) Quantitative analysis of JAK2, p-JAK2, STAT3 and p-STAT3 signaling pathway by immunohistochemistry. $^{\#\#\#\#}p < 0.0001$ versus the normal group, $^{*}p < 0.05$, and $^{****}p < 0.0001$ versus the model group.

ing these results. First, although we successfully validated the involvement of the JAK2-STAT3 signaling pathway at the protein level *in vivo*, our transcriptomic analysis highlighted other significant inflammatory cascades. The specific roles of these alternative pathways and their potential crosstalk during BBR-CA treatment remain to be experimentally verified. Second, despite being a standard preclinical tool, the DSS-induced acute colitis mouse model does not fully capture the chronic and complex immune-mediated pathogenic characteristics of human UC. This discrepancy may limit the direct clinical translatability of our findings, necessitating future validation using chronic or spontaneous animal models. Third, our *in vivo* pharmacokinetic evaluations were conducted using healthy rats to evaluate drug absorption. Although we used an *in vitro* inflammatory cell model to simulate disease-associated intestinal permeability, *in vitro* monocultures could not fully replicate the complex *in vivo* gastrointestinal microenvironment of active UC, which involves degradation of the mucus layer, massive immune cell infiltration, and altered intestinal motility. Therefore, the *in vivo* absorption dynamics and bioavailability of BBR-CA in the symptomatic disease state may differ from the current healthy-state pharmacokinetic observations. Finally, considering that BBR exerts therapeutic effects via modulation of the gut microbiota, the absence of microbiome profiling in our study hinders the comprehensive elucidation of the BBR-CA pharmacological network. Future studies should address these limitations to fully elucidate the clinical value and precise mechanisms of BBR-CA.

6. Conclusions

BBR-CA co-crystals enhanced the intestinal absorption and bioavailability of BBR by regulating the JAK2-STAT3 signaling pathway, resulting in decreased inflammation and increased intestinal epithelial tight junctions to alleviate UC.

Abbreviations

BBR, Berberine; CA, Cinnamic acid; BBR-CA, Berberine- cinnamic acid co-crystal; UC, Ulcerative colitis; SAZ, salazosulfapyridine; LPS, lipopolysaccharide; DAI, disease activity index; SEM, Scanning electron microscopy; DSS, Dextran sulfate sodium salt; IR, Infrared radiation; FTIR, Fourier Transform Infrared Spectroscopy; DSC, Differential scanning calorimetry; MRT, Mean residence time; AUC, Area under the curve; P_{app}, Apparent permeation coefficient; GSEA, Gene Set Enrichment Analysis; GO, Gene Ontology; KEGG, Kyoto Encyclopedia of Genes and Genomes.

Availability of Data and Materials

Further materials related to this study are available from the corresponding authors upon reasonable request.

Author Contributions

ML and CH designed the research study. ML and WG performed the research. YH, YY, and DY participated in the animal and cell experiments and provided assistance and advice. ML and ST analyzed the data. ML, CH, and ST wrote the manuscript. All authors contributed to editorial changes in the manuscript. All authors read and approved the final manuscript. All authors have participated sufficiently in the work and agreed to be accountable for all aspects of the work.

Ethics Approval and Consent to Participate

This study complies with the guidelines for the Ethical Review of Laboratory Animal Welfare of the People's Republic of China (GB/T 35892-2018). The research protocol was approved by the Laboratory Animal Ethics Committee of Anhui University of Chinese Medicine (AHUCM-mouse-2022128; AHUCM-rats-2022086). The study was carried out in accordance with the ARRIVE guidelines.

Acknowledgment

Not applicable.

Funding

This research was funded by the key project of the Anhui Provincial Department of Education (2022AH040077), the National Natural Science Foundation of China (82304542), Foundation of Anhui Provincial Key Laboratory of Chinese Medicinal Formula (2024AKLCMF07), The Open Fund of High-level Key Discipline of Chemistry of Chinese Medicine of the State Administration of Traditional Chinese Medicine, Anhui University of Chinese Medicine (HKDCCM2024017), Scientific Research Team Program of Anhui Colleges and Universities (2022AH010036), Excellent Youth Project of Anhui Provincial Department of Education (2024AH030034).

Conflicts of Interest

The authors declare no conflicts of interest.

Supplementary Material

Supplementary material associated with this article can be found, in the online version, at https://doi.org/10.31083/IJP49188.

References

[1] Tatiya-Aphiradee N, Chatuphonprasert W, Jarukamjorn K. Immune response and inflammatory pathway of ulcerative colitis. Journal of Basic and Clinical Physiology and Pharmacology. 2018; 30: 1–10. https://doi.org/10.1515/jbcpp-2018-0036

[2] Neurath MF. Cytokines in inflammatory bowel disease. Nature Reviews. Immunology. 2014; 14: 329–342. https://doi.org/10.1038/nri3661

[3] Vuddanda PR, Chakraborty S, Singh S. Berberine: a potential phytochemical with multispectrum therapeutic activities. Expert

Opinion on Investigational Drugs. 2010; 19: 1297–1307. https://doi.org/10.1517/13543784.2010.517745
[4] Li C, Xi Y, Li S, Zhao Q, Cheng W, Wang Z, et al. Berberine ameliorates TNBS induced colitis by inhibiting inflammatory responses and Th1/Th17 differentiation. Molecular Immunology. 2015; 67: 444–454. https://doi.org/10.1016/j.molimm.2015.07.013
[5] Jamshaid F, Dai J, Yang LX. New Development of Novel Berberine Derivatives against Bacteria. Mini Reviews in Medicinal Chemistry. 2020; 20: 716–724. https://doi.org/10.2174/1389557520666200103115124
[6] Mortazavi H, Nikfar B, Esmaeili SA, Rafieenia F, Saburi E, Chaichian S, et al. Potential cytotoxic and anti-metastatic effects of berberine on gynaecological cancers with drug-associated resistance. European Journal of Medicinal Chemistry. 2020; 187: 111951. https://doi.org/10.1016/j.ejmech.2019.111951
[7] Ayati SH, Fazeli B, Momtazi-Borojeni AA, Cicero AFG, Pirro M, Sahebkar A. Regulatory effects of berberine on microRNome in Cancer and other conditions. Critical Reviews in Oncology/Hematology. 2017; 116: 147–158. https://doi.org/10.1016/j.critrevonc.2017.05.008
[8] Fatahian A, Haftcheshmeh SM, Azhdari S, Farshchi HK, Nikfar B, Momtazi-Borojeni AA. Promising Anti-atherosclerotic Effect of Berberine: Evidence from In Vitro, In Vivo, and Clinical Studies. In Pedersen SHF (eds.) Reviews of Physiology, Biochemistry and Pharmacology (pp. 83–110). Springer International Publishing: Cham. 2020.
[9] Feng X, Sureda A, Jafari S, Memariani Z, Tewari D, Annunziata G, et al. Berberine in Cardiovascular and Metabolic Diseases: From Mechanisms to Therapeutics. Theranostics. 2019; 9: 1923–1951. https://doi.org/10.7150/thno.30787
[10] Liang Y, Xu X, Yin M, Zhang Y, Huang L, Chen R, et al. Effects of berberine on blood glucose in patients with type 2 diabetes mellitus: a systematic literature review and a meta-analysis. Endocrine Journal. 2019; 66: 51–63. https://doi.org/10.1507/endocrj.EJ18-0109
[11] Kuo CL, Chi CW, Liu TY. The anti-inflammatory potential of berberine in vitro and in vivo. Cancer Letters. 2004; 203: 127–137. https://doi.org/10.1016/j.canlet.2003.09.002
[12] Liu CS, Zheng YR, Zhang YF, Long XY. Research progress on berberine with a special focus on its oral bioavailability. Fitoterapia. 2016; 109: 274–282. https://doi.org/10.1016/j.fitote.2016.02.001
[13] Xiong J, Xu D, Zhang H, Shi Y, Wu X, Wang S. Improving the Solubility and Bioavailability of Progesterone Cocrystals with Selected Carboxylic Acids. Pharmaceutics. 2024; 16: 816. https://doi.org/10.3390/pharmaceutics16060816
[14] Gao Z, Liu S, Sun CC. Complexation with aromatic carboxylic acids expands the solid-state landscape of berberine. International Journal of Pharmaceutics. 2022; 617: 121587. https://doi.org/10.1016/j.ijpharm.2022.121587
[15] He Y, Chen S, Li M, Gao Y, Feng H, Umar Q, et al. Novel co-crystal of 3-methylcinnamic acid with berberine (1:1): synthesis, characterization, and intestinal absorption property. Drug Development and Industrial Pharmacy. 2023; 49: 617–627. https://doi.org/10.1080/03639045.2023.2259460
[16] Xiao Y, Biao YN, Wang Y, Liu CX, Li L, Gao JM, et al. The effect of xieli decoction on inflammatory factors and intestinal mucosal barrier injury in mice with ulcerative colitis. *Pharmacology and Clinics of Chinese Materia Medica*. 2023; 39: 1–6. https://doi.org/10.13412/j.cnki.zyyl.20230223.004 (In Chinese)
[17] Sun P, Li S, Teng J, Zhang W, Li C, Zhang C. Identification of novel bioactive constituents from traditional decoction of jiaotai-Wan based on "co-decoction reaction" and comparative analysis with formula granules. Journal of Chromatography. B, Analytical Technologies in the Biomedical and Life Sciences. 2026; 1274: 124977. https://doi.org/10.1016/j.jchromb.2026.124977
[18] Guzman JD. Natural cinnamic acids, synthetic derivatives and hybrids with antimicrobial activity. Molecules. 2014; 19: 19292–19349. https://doi.org/10.3390/molecules191219292
[19] Sadeghi S, Davoodvandi A, Pourhanifeh MH, Sharifi N, ArefNezhad R, Sahebnasagh R, et al. Anti-cancer effects of cinnamon: Insights into its apoptosis effects. European Journal of Medicinal Chemistry. 2019; 178: 131–140. https://doi.org/10.1016/j.ejmech.2019.05.067
[20] Natella F, Nardini M, Di Felice M, Scaccini C. Benzoic and cinnamic acid derivatives as antioxidants: structure-activity relation. Journal of Agricultural and Food Chemistry. 1999; 47: 1453–1459. https://doi.org/10.1021/jf980737w
[21] Gao W, Li Y, Chen L, Yang W, He Y, Yang Y, et al. Berberine–cinnamic acid co-crystal effect in ameliorating hyperlipidemia might be regulated through the PI3K/AKT/mTOR/SREBP-1 signaling pathway. FEBS Open Bio. 2026; 16: 145–160. https://doi.org/10.1002/2211-5463.70115
[22] Liu Y, Dong Y, Shen W, DU J, Sun Q, Yang Y, et al. Platycodon grandiflorus polysaccharide regulates colonic immunity through mesenteric lymphatic circulation to attenuate ulcerative colitis. Chinese Journal of Natural Medicines. 2023; 21: 263–278. https://doi.org/10.1016/S1875-5364(23)60435-2
[23] Artursson P, Karlsson J. Correlation between oral drug absorption in humans and apparent drug permeability coefficients in human intestinal epithelial (Caco-2) cells. Biochemical and Biophysical Research Communications. 1991; 175: 880–885. https://doi.org/10.1016/0006-291x(91)91647-u
[24] Hu JCE, Weiß F, Bojarski C, Branchi F, Schulzke JD, Fromm M, et al. Expression of tricellular tight junction proteins and the paracellular macromolecule barrier are recovered in remission of ulcerative colitis. BMC Gastroenterology. 2021; 21: 141. https://doi.org/10.1186/s12876-021-01723-7
[25] Kuo WT, Odenwald MA, Turner JR, Zuo L. Tight junction proteins occludin and ZO-1 as regulators of epithelial proliferation and survival. Annals of the New York Academy of Sciences. 2022; 1514: 21–33. https://doi.org/10.1111/nyas.14798
[26] Kuo WT, Shen L, Zuo L, Shashikanth N, Ong MLDM, Wu L, et al. Inflammation-induced Occludin Downregulation Limits Epithelial Apoptosis by Suppressing Caspase-3 Expression. Gastroenterology. 2019; 157: 1323–1337. https://doi.org/10.1053/j.gastro.2019.07.058
[27] Mrsny RJ, Brown GT, Gerner-Smidt K, Buret AG, Meddings JB, Quan C, et al. A key claudin extracellular loop domain is critical for epithelial barrier integrity. The American Journal of Pathology. 2008; 172: 905–915. https://doi.org/10.2353/ajpath.2008.070698
[28] Pandurangan AK, Ismail S, Saadatdoust Z, Esa NM. Allicin Alleviates Dextran Sodium Sulfate- (DSS-) Induced Ulcerative Colitis in BALB/c Mice. Oxidative Medicine and Cellular Longevity. 2015; 2015: 605208. https://doi.org/10.1155/2015/605208
[29] de Faria FM, Luiz-Ferreira A, Socca EAR, de Almeida ACA, Dunder RJ, Manzo LP, et al. Effects of Rhizophora mangle on Experimental Colitis Induced by TNBS in Rats. Evidence-Based Complementary and Alternative Medicine. 2012; 2012: 753971. https://doi.org/10.1155/2012/753971
[30] Suzuki T. Regulation of the intestinal barrier by nutrients: The role of tight junctions. Animal Science Journal. 2020; 91: e13357. https://doi.org/10.1111/asj.13357
[31] Kim MS, Kim JY. Cinnamon subcritical water extract attenuates intestinal inflammation and enhances intestinal tight junction in a Caco-2 and RAW264.7 co-culture model. Food & Function. 2019; 10: 4350–4360. https://doi.org/10.1039/c9fo00302a
[32] Dong Y, Fan H, Zhang Z, Jiang F, Li M, Zhou H, et al. Berberine ameliorates DSS-induced intestinal mucosal barrier dysfunction

through microbiota-dependence and Wnt/β-catenin pathway. International Journal of Biological Sciences. 2022; 18: 1381–1397. https://doi.org/10.7150/ijbs.65476

[33] Zhang X, Zhao Y, Xu J, Xue Z, Zhang M, Pang X, et al. Modulation of gut microbiota by berberine and metformin during the treatment of high-fat diet-induced obesity in rats. Scientific Reports. 2015; 5: 14405. https://doi.org/10.1038/srep14405

[34] Zhao DK, Wen ST, Niu J, Wang Q, Mi H, Liu FB. Exploring the Therapeutic Mechanism of Artesunate Against Ulcerative Colitis via Network Pharmacology and Molecular Docking. International Journal of Pharmacology. 2025; 21: 295–316. https://doi.org/10.3923/ijp.2025.295.316

[35] Verstockt B, Alsoud D, van Oostrom J, Verstockt S, Smith J, Stylli J, et al. Drug tissue concentration and STAT3 modulation as determinants of tofacitinib response in ulcerative colitis. Journal of Crohn's & Colitis. 2025; 19: jjaf063. https://doi.org/10.1093/ecco-jcc/jjaf063

[36] Zhao Y, Luan H, Jiang H, Xu Y, Wu X, Zhang Y, et al. Gegen Qinlian decoction relieved DSS-induced ulcerative colitis in mice by modulating Th17/Treg cell homeostasis via suppressing IL-6/JAK2/STAT3 signaling. Phytomedicine. 2021; 84: 153519. https://doi.org/10.1016/j.phymed.2021.153519

[37] Li Y, Wu Y, Liang J, Chen P, Xu S, Wang Y, et al. Ligustilide Suppresses Macrophage-Mediated Intestinal Inflammation and Restores Gut Barrier via EGR1-ADAM17-TNF-α Pathway in Colitis Mice. Research. 2025; 8: 0864. https://doi.org/10.34133/research.0864

[38] Meng T, Li X, Li C, Liu J, Chang H, Jiang N, et al. Natural products of traditional Chinese medicine treat atherosclerosis by regulating inflammatory and oxidative stress pathways. Frontiers in Pharmacology. 2022; 13: 997598. https://doi.org/10.3389/fphar.2022.997598

[39] Bastida G, Mínguez A, Nos P, Moret-Tatay I. Immunoepigenetic Regulation of Inflammatory Bowel Disease: Current Insights into Novel Epigenetic Modulations of the Systemic Immune Response. Genes. 2023; 14: 554. https://doi.org/10.3390/genes14030554

[40] Zhao Q, Luan X, Zheng M, Tian XH, Zhao J, Zhang WD, et al. Synergistic Mechanisms of Constituents in Herbal Extracts during Intestinal Absorption: Focus on Natural Occurring Nanoparticles. Pharmaceutics. 2020; 12: 128. https://doi.org/10.3390/pharmaceutics12020128